Chinese Chemical Letters 35 (2024) 109285

Contents lists available at ScienceDirect

Chinese Chemical Letters

journal homepage: www.elsevier.com/locate/cclet

In situ constructing (MnS/Mn_2SnS_4)@N,S-ACTs heterostructure with superior Na/Li-storage capabilities in half-cells and pouch full-cells

Dai-Huo Liu[a,d], Ao Wang[a,d], Hong-Yan Lü[b,*], Xing-Long Wu[b,c], Dan Luo[d], Wen-Hao Li[b], Jin-Zhi Guo[c], Haozhen Dou[d], Qianyi Ma[e], Zhongwei Chen[d,e,*]

[a] *Key Laboratory of Green Chemical Media and Reaction, Ministry of Education, Collaborative Innovation Center of Henan Province for Fine Chemicals Green Manufacturing of Fine Chemicals, School of Chemistry and Chemical Engineering, Henan Normal University, Xinxiang 453007, China*
[b] *Faculty of Chemistry, Northeast Normal University, Changchun 130024, China*
[c] *MOE Key Laboratory for UV Light-Emitting Materials and Technology, Northeast Normal University, Changchun 130024, China*
[d] *Power Battery and Systems Research Center, Dalian Institute of Chemical Physics, Chinese Academy of Sciences, Dalian 116023, China*
[e] *Department of Chemical Engineering, Waterloo Institute for Nanotechnology, Waterloo Institute for Sustainable Energy, Waterloo University, Waterloo, ON N2L 3G1, Canada*

ARTICLE INFO

Article history:
Received 18 August 2023
Revised 26 September 2023
Accepted 6 November 2023
Available online 8 November 2023

Keywords:
(MnS/Mn_2SnS_4)@N,S-ACTs
Heterostructure
Long cycling life
Na-/Li-ion half cells
Pouch full cells

ABSTRACT

Effective design of nanoheterostructure anode with high ion/electron migration kinetics can give electrode with superior electrochemical performance. However, the design and preparation of nanoheterostructure composites with high-capacity and long cycling life in half and pouch full cells remain a big challenge. Here, a novel micro-pore MnS/Mn_2SnS_4 heterostructure nanowire were *in situ* encapsulated into the N and S elements co-doped amorphous carbon tubes (abbreviated as (MnS/Mn_2SnS_4)@N,S-ACTs) and showed superior energy storage properties in Na-/Li-ion half cells and pouch full cells. The Na-/Li-storage capabilities improvement are attribute to the strong synergistic effect between MnS/Mn_2SnS_4 heterostructure and N,S-ACTs protective layer, the former induces an local built-in electric field between Mn_2SnS_4 and MnS during charging/discharging, accelerating interfacial ion/electron diffusion dynamics, the latter effective maintains the morphology and volume evolution during Na^+/Li^+ charging/discharging, achieving a long-term cycling stability (*e.g.*, high discharge capacity of 79.2 mAh/g with the capacity retention of 79.3% can be gained after 2200 cycles at 3 C in (MnS/Mn_2SnS_4)@N,S-ACTs//$LiFePO_4$ pouch full cells; a high capacity of ~34 mAh/g at 10 C can be got with a Coulombic efficiency of 100% after 1000 cycles in pouch (MnS/Mn_2SnS_4)@N,S-ACTs//$Na_3V_2(PO_4)_2O_2F$ full cells.

The traditional nonrenewable fossil fuel depletion led to environmental pollution and greenhouse effect, there is an urgent demand for many renewable green energy sources to power new energy vehicles (NEVs) [1,2]. Recently, NEVs are becoming more and more important as European countries such as France, the Netherlands and Germany etc. have put forward a timetable to prohibit selling fuel cars. As a major device for NEVs, Li-ion batteries (LIBs) have played an important role due to its superior energy storage performance in the fields of portable electronics and NEVs [1,3]. In contrast to LIBs, the cost-effective Na-ion batteries (NIBs) have attracted increasingly attention in smart electric grids [4,5]. In order to better satisfy the increasing needs for high-energy/power density and long cycling life, it is an urgent task to designed superior electrode with outstanding rate capacity and long cycle life in both half and pouch full cells for LIBs/NIBs [6].

Great interests have been devoted to research new electrode materials with high specific capacity (C_s) and superior cycling stability in the half/full-cells of both NIBs and LIBs [7,8]. The rational interface engineering and morphology-controlled synthesis of new electrodes with superior dynamics and electrochemical performance are highly satisfactory [9]. In this respect, heterostructure hybrid materials exhibited huge potential in the fields of high-speed electronics, optoelectronics devices and energy storage devices due to their local built-in electric field at heterointerface, which will boost the Na^+/Li^+ diffusion kinetics and hence obtain ultra-fast charge-transfer [10,11]. For example, a couple nanocrystals with different band gaps can promote charge transport and improve the surface reaction kinetics because of the internal electric field at heterointerface [12,13], which will impel the charge-transfer kinetics and enhance electronic conductivity [7,10,14,15].

* Corresponding authors.
E-mail addresses: luhy836@nenu.edu.cn (H.-Y. Lü), zhwchen@uwaterloo.ca (Z. Chen).

https://doi.org/10.1016/j.cclet.2023.109285
1001-8417/

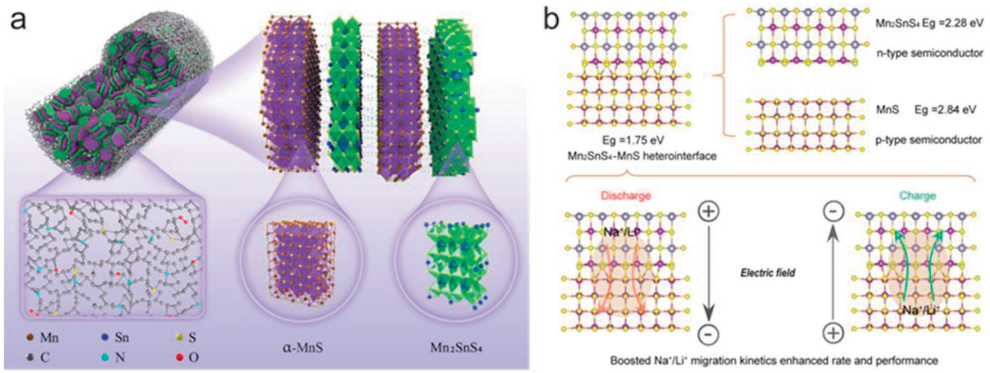

Scheme 1. (a) Schematic of the well-designed (MnS/Mn_2SnS_4)@N,S-ACTs heterostructure. (b) Heterostructure achieved lower band gap and induced improved ionic/electron migration kinetics *via* the local built-in electric field.

From the viewpoint of promoting the charge-transfer kinetics, improving electronic conductivity and alleviating volume change of electrode materials, it could be a feasible micro-pore nanocomposite with by using the heterostructure MnS/Mn_2SnS_4 (henceforth denoted as *h*-MMS). Herein, the micro-pore *h*-MMS nanowire were *in situ* encapsulated into the N and S elements co-doped amorphous carbon tubes (N,S-ACTs), a porous heterostructured (MnS/Mn_2SnS_4)@N,S-ACTs (abbreviated as *h*-MMS@N,S-ACTs) nanocomposite was successfully prepared. As expected, the designed *h*-MMS@N,S-ACTs electrode exhibited preeminent high-rate ability and stable long-cycle life in half and pouch full cells of NIBs/LIBs.

The well-designed nanohybrid for the *h*-MMS@N,S-ACTs heterostructure is presented in Scheme 1a, numerous *h*-MMS heterostructure nanoparticles are encapsulated into one dimensional N,S-ACTs, a mass of *h*-MMS heterostructures are firmly anchored on the internal wall of N,S-ACTs. The rich meso–pore derived from the accumulation between *h*-MMS heterostructures, which can effective relieve the volume fluctuation during repetitive Na^+/Li^+ insertion/desertion reactions. The outer N,S-ACTs layer have five functions: (1) The flexible N,S-ACTs can well maintain the integrity of morphology and nanostructural during cycling; (2) It can boost the conductivity and diffusion kinetics of *h*-MMS heterostructure; (3) It can effective relieve the volume change during Na^+/Li^+ insertion and de-intercalation; (4) The N,S-codoped amorphous carbon tubes has a better wettability to Na^+/Li^+ and electrolyte; (5) Benefiting the closely close between *h*-MMS heterostructure and flexible N,S-ACTs, the *h*-MMS@N,S-ACTs heterostructures would achieve fast-charging capability. Furthermore, the crystalline structures of rock-salt-type MnS and Mn_2SnS_4 are presented in Scheme 1a, they have been attracting tremendous interests in anode candidate for advanced second cells because they own high C_s and superior electrochemical performances. MnS possesses a high theoretical C_s of 616 mAh/g, as well as eco-friendliness, crustal abundance, and high cost-effectiveness. And tin-based sulfide has rapid Li^+/Na^+-ion migration capability and excellent electrochemical activity.

The architectural features of designed *h*-MMS heterostructure were analyzed from a theoretical perspective of density functional theory (DFT). The *h*-MMS@N,S-ACTs heterostructures possesses a lower band gap (E_g, 1.75 eV) than that of the single counterpart of Mn_2SnS_4 (2.28 eV) and MnS (2.84 eV) (Scheme 1b and Fig. S1 in Supporting information), the nature of the unique *h*-MMS heterostructure could realize comprehensive improvement for fast-charging and cycling stability in second batteries. As shown in Figs. S1d and e, the h-MMS@N,S-ACTs electrode has a lower charge transfer resistances (R_{ct}) and faster diffusion kinetics than MnS and Mn_2SnS_4, indicating better conductivity, which is consistent with the decrease of band gap from the DFT calculations results. Besides, the atomic configuration and related electronic structure are thought to determine electrochemical performances, including the migratory behavior of electrons and ions. For example, Fig. S2 (Supporting information) of TDOS results show possible formation of MnS/Mn_2SnS_4 heterostructure. To estimate the charges that transfer to interface between MnS and Mn_2SnS_4, Bader charge analysis was also applied [16,17]. We found that there is a net charge of 1.47 electrons transfer from the Mn_2SnS_4 to MnS (Figs. S2 and S3 in Supporting information), the nonequilibrium charge distribution can generate a local built-in electric field at the interface between Mn_2SnS_4 and MnS during charging/discharging (Scheme 1b), which would offer an extra driving force to boost the Na^+/Li^+ migration kinetics, and hence obtain superior rate performance, which will be verified *via* subsequently electrochemical characterizations.

The special nanostructure and kinetics advantages of designed heterostructure materials motivate us to further prepare it. The detailed preparation processes for the *h*-MMS@N,S-ACTs heterostructure are illustrated as below. Firstly, the template of coaxial $MnO_2@SnO_2$ nanotubes (NTs) was synthesized *via* two-step simple hydrothermal method according to previously report [18,19]. Secondly, the coaxial $MnO_2@SnO_2$ NTs are polydopamine (PDA) coated through a liquid phase polymerization. Lastly, the porous MnS/Mn_2SnS_4 nanoheterostructures are *in situ* coated inside amorphous N,S-ACTs by subsequently carbonization and sulfurization processes. The detailed synthesis procedures and corresponding characterizations of the precursors are presented in the supporting information (Figs. S4-S9 in Supporting information).

The crystalline phase and purity of as prepared *h*-MMS@N,S-ACTs heterostructure were first analyzed *via* X-ray diffraction (XRD). As shown in Fig. 1a, all the peaks could be well indexed to the standard cards of cubic α-MnS and orthorhombic Mn_2SnS_4, and no any other impurities are observed. As shown in Fig. 1b, the Raman spectrum data further confirms the existence of MnS and Mn_2SnS_4 in the *h*-MMS@N,S-ACTs heterostructure. There are two characteristic peaks assigned to MnS [20] and Mn_2SnS_4 [21] at 646.2 cm^{-1} and 287.5 cm^{-1}, respectively, the ratio both disorder (D) and graphitic (G) bands in N,S-ACTs is ~1.1, illustrates the disordered and defective nature of N,S-ACTs [22]. In addition, the composition and valence state of the *h*-MMS@N,S-ACTs heterostructure is determined by X-ray photoelectron spectroscopy (XPS, Fig. S10 in Supporting information) [23,24], which are detail analyzed in Supporting information.

Microstructure and morphology of the prepared *h*-MMS@N,S-ACTs heterostructure were characterized by scanning electron microscopy (SEM), (high-resolution) transmission electron microscopy (TEM, HRTEM) and energy-dispersive X-ray spectroscopy (EDS). Fig. 1c shows that *h*-MMS@N,S-ACTs is a typical 1D nanowire with 0.5–

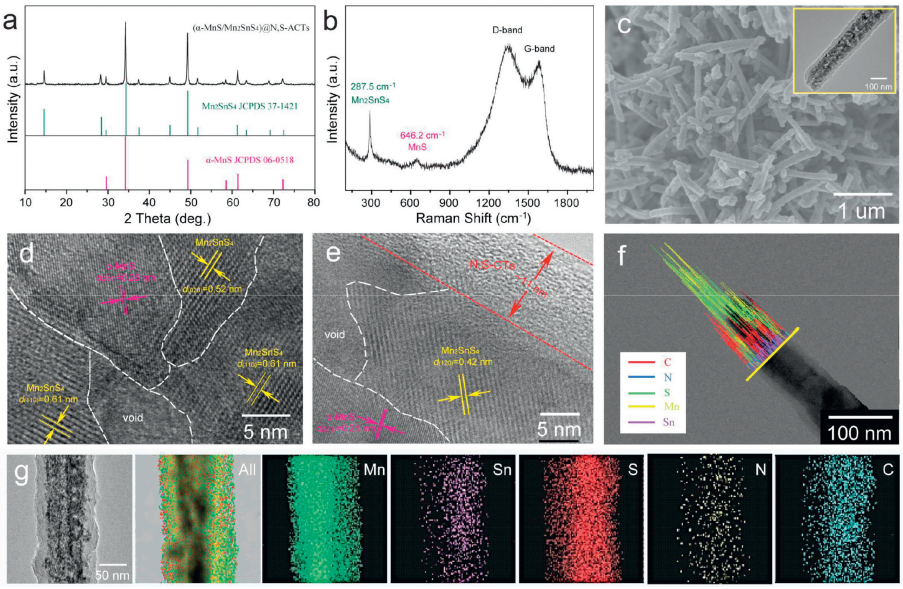

Fig. 1. (a) X-ray diffraction pattern, (b) Raman spectrum, (c) SEM (inset is TEM of single one), (d, e) HRTEM, (f) EDS line-scan and (g) elementary mapping of (MnS/Mn_2SnS_4)@N,S-ACTs heterostructures.

2 μm in length and ~100 nm in diameter. The inset indicates that the MnS and Mn_2SnS_4 is anchored in the N,S-ACTs, a lot of voids are formed between MnS/Mn_2SnS_4 nano heterostructures, which would be very beneficial to accommodate the successive volume changes of active electrode materials as cycling [25]. Figs. 1d and e prove that *h*-MMS@N,S-ACTs is a typical nano heterostructure nanohybrid. The center region of *h*-MMS@N,S-ACTs reveals that the lattice spacing of 0.26 and 0.21 nm, which correspond to the (200) and (211) planes of MnS, respectively. The 0.52, 0.61 and 0.42 nm are assigned to the (020), (110) and (120) planes of Mn_2SnS_4, respectively. For single *h*-MMS@N,S-ACTs nanowire shows that the Mn, S, Sn elements are located in the inner of N,S-ACTs, which are also demonstrated *via* EDS mappings, indicating the even distribution of all elements (Figs. 1f and g). Brunauer-Emmett-Teller fitting (Fig. S11a in Supporting information) reveals a higher area (SSA) of 466.7 m^2/g for *h*-MMS@N,S-ACTs, which own rich micro/mesopores of 1.5–32 nm from Barrett-Joyner-Halenda calculation (Fig. S11b in Supporting information), the micro/mesopores may be derived from the stacking between *h*-MMS NPs in N,S-ACTs. The higher SSA and micro/mesopores features can offer fast ionic/electronic migration pathways and abundant active sites to boost the Na-/Li-storage capability. The contents of Mn_2SnS_4, MnS and N,S-ACTs in *h*-MMS@N,S-ACTs are confirmed to be 54.1, 24.8 and 21.1 wt%, respectively, *via* the thermogravimetric analysis (Fig. S12 in Supporting information) and inductively coupled plasma-atomic emission spectroscopy data. After dissolving the *h*-MMS in h-MMS@N,S-ACTs, elemental analysis obtains that N, C and S contents of N,S-ACTs are 4.6, 55.4 and 13.3 wt%, respectively (Table S1 in Supporting information), proving the higher doping contents of N and S, the N,S-ACTs presents a typical nanotube shape (Fig. S13 in Supporting information).

The Na-storage ability of as-prepared *h*-MMS@N,S-ACTs heterostructure was first inspected in half cells with Na foil as counter electrodes. The cyclic voltammetry (CV) testing was tested in 0.005–3.0 V at 0.1 mV/s (Fig. 2a). The reversible anodic peaks located at around 0.88 V may be assigned to the sodiation. During the anodic scan, a weak peak located at ~0.66 V is detected, which corresponds to the desodiation process, there is a high voltage plateau at around 2.17 V, which suggests that the Mn^{2+} ions are reoxidized to Mn^{3+} or Mn^{4+} [26,27]. The *h*-MMS@N,S-ACTs heterostructure deliver excellent rate performance (Fig. 2b), benefiting from unique heterostructure deliver excellent rate performance (Fig. 2b), benefiting from unique nanoarchitecture. The Na-storage property of *h*-MMS@N,S-ACTs electrode is obvious superior to the bulk *h*-MMS, including C_s, rate ability, Coulombic efficiency (CE), electrochemical reversibility and cycling life. As shown in Fig. S14 (Supporting information), the calculated D_s values of h-MMS@N,S-ACTs ($1 \times 10^{-9.66}$ cm^2/s) is higher than those of MnS ($1 \times 10^{-10.04}$ cm^2/s) and Mn_2SnS_4 ($1 \times 10^{-9.90}$ cm^2/s), demonstrating the h-MMS@N,S-ACTs electrode possesses a faster Na^+/Li^+ migration kinetics. For example, Na-storage capacity is up to ~600 mA h/g at 0.1 A/g; Even at a ultra-high rate of 15 A/g, it still deliver ~200 mAh/g, the C_s can recover to ~540 mAh/g when the rate come back to 0.1 A/g; A highly reversible galvanostatic charge/discharge (GCD) profiles at 0.1 A/g can be achieved in Fig. 2c, the curves are overlapped from 2nd to 5th cycles, which agree with CV curves (Fig. 2a), and the CE of first cycle reached ~70%. Significantly, the *h*-MMS@N,S-ACTs electrode showed superior cycling stability (Fig. 2d), a high C_s of ~200 mAh/g at an ultrahigh rate of 7.5 A/g can be obtained with a slight capacity attenuation after 1000 cycles. The h-MMS@N,S-ACTs electrode shows better cycling and rate performance than most reported Mn/Sn-based anodes for SIBs (Table S3 in Supporting information).

Na-ion pouch full cells of *h*-MMS//NVPOF (*h*-MMS@N,S-ACTs anode abbreviated as *h*-MMS, $Na_3V_2(PO_4)_2O_2F$ cathode abbreviated as NVPOF for pouch full-cell writing) were assembled to explore its feasibility in practical applications. The rate GCD curves of *h*-MMS//NVPOF full cells are exhibited in Fig. 3a, it have two redox plateaus (3.6/2.5 V and 1.7/3.1 V for cathodic and anodic scanning), which agree with the CV profiles (Fig. S15 in Supporting information), the cathodic/anodic curves from 2^{nd} to 5^{th} are almost overlapped in the CV curves of pouch full cells, indicating a highly reversible redox processes [28]. Additionally, the shapes of the GCD of *h*-MMS//NVPOF pouch full cells are well retained at various C rates as shown in Fig. 3a. Its excellent rate capabilities are benefiting from the well-design *h*-MMS@N,S-ACTs anode (Fig. 3b). For instance, a high C_s of 105 mAh/g at 0.5 C is obtained with a high CE of 91% in the first cycle; the discharge C_s still remain ~43 mAh/g even at an very high rate of 80 C (45 s completed a discharge); and the CE values at various C-rates are close to 100%. Apart from superior rate ability, *h*-MMS//NVPOF pouch full cells also show long-term cycling capability. As shown in Fig. 3c, there is a high C_s of

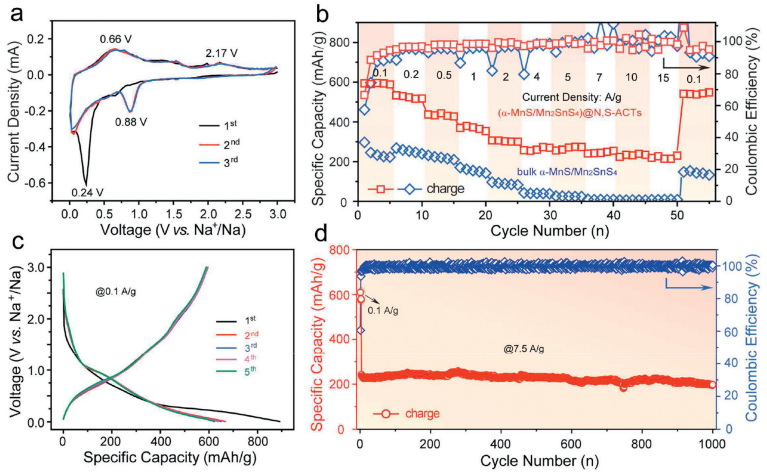

Fig. 2. (a) Electrochemical characterizations for NIBs half cells. (a) CV curves at a scan rate of 0.1 mV/s of *h*-MMS@N,S-ACTs electrode. (b) The GCD curves of *h*-MMS@N,S-ACTs electrode. (c) The comparison of rate performance of *h*-MMS@N,S-ACTs and bulk *h*-MMS NWs electrodes. (d) The cycle performance after firstly three cycles at 0.1 A/g of *h*-MMS@N,S-ACTs electrodes.

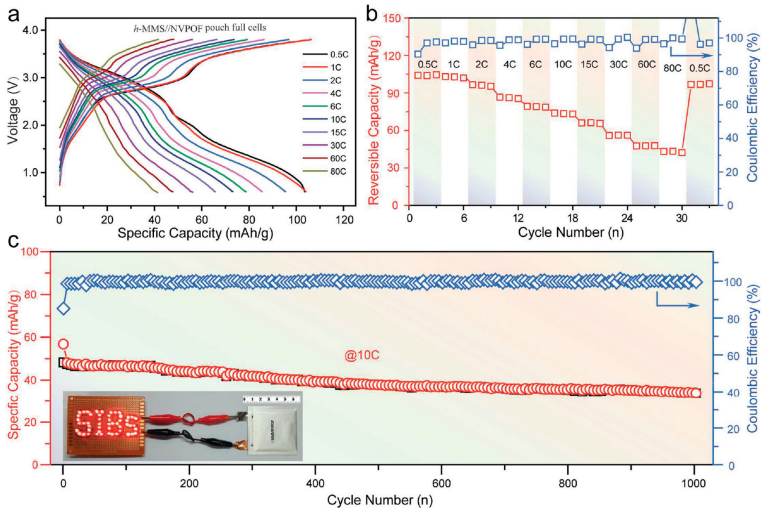

Fig. 3. Electrochemical characterizations for Na-ion pouch full cells. (a) CV curves at a scan rate of 0.1 mV/s, (b) rate performance and (c) long cycle life after firstly three cycles at 0.5 C of *h*-MMS//NVPOF full cell. Inset of (c) shows that one fabricated Na-ion pouch full cell can lighten on a series LED.

34 mAh/g over 1000 cycles at a high C-rate of 10 C with a high CE of 100%, implying a high stability of electrochemical reaction in *h*-MMS//NVPOF pouch full cells. The assembled 6 cm × 6 cm lighten the light-emitting diode (LED) bulbs.

Apart from the superior Na-ion half and pouch full cell properties, the Li-storage properties of *h*-MMS@N,S-ACTs anode in coin-type half cells with Li-foil as counter electrodes is also detail explored between 0.005 V and 2.5 V. The CV was tested at 0.1 mV/s (Fig. 4a). In the first cathodic scan, two obvious peaks at 1.68 and 0.76 V are completely different from second and subsequent cycles, indicating the SEI filmformation. The reversible cathodic peaks located at around 0.42, 0.9, 1.23, 1.35 V may be assigned to the lithiation reaction and at around 0.42 V may be assigned to alloy reactions between Sn and Li^+ to form Li_xSn [14,29]. During the anodic scan, a weak and wide peak centered at ~0.57 V is seen in the initial and the following cycles, which corresponds to the dealloying process of Li_xSn [29]. The other two peaks at 1.0 and 1.3 V are assigned to the delithiation reaction [30]. The second and the subsequent CV profiles are almost overlapped, implying superior reversibility and structural stability of redox reaction of *h*-MMS@N,S-ACTs anode. Indeed, the *h*-MMS@N,S-ACTs also exhibits superior rate performance, the 1st reversible capacity (R_c) as high as 894.5 mAh/g with the 1st CE of 71.4% at 0.1 A/g (Fig. 4b). The R_c are extremely slow decrease as current density increase from 0.1 A/g to 15 A/g, even at 15 A/g, the R_c values still remain at 443.9 mAh/g with the capacity retention of 49.6% calculated from 1st cycle. Importantly, the R_c can recover to ~900 mAh/g when current densities return to 0.1 A/g after various current densities, illustrating the better reversibility of electrochemical reaction. The superior electrochemical performance should be profit from unique nanoheterostructure with the protective layer of N,S- ACTs, because the N,S-ACTs can not only offer high conductivity and prevent the agglomeration between the *h*-MMS heterostructures, but also effectively capture the Li_2S_x ($4 \leq x \leq 8$) in the N,S-ACTs to avoid the dissolution of polysulfides in electrolyte [24]. On the contrary, the bulk *h*-MMS electrode shows very poor rate capability, lower 1st CE (~52%) and a larger fluctuation of CE at various rates due to itself poor conductivity and agglomeration between bare *h*-MMS NPs during charging/discharge.

In order to verify the superior Li-storage ability, its pseudocapacitive behavior is investigated by fitting CV curves (Fig. S16a in Supporting information). When the *b*-value is close to 1, it is believe that the reaction is dominated by the pseudocapaaitance. After calculation, the *b*-value of peak 1, 2, 3 and 4 are 0.74, 0.81, 0.96 and 0.95, respectively (Fig. S16b in Supporting information), indicating that the electrochemical reactions of *h*-MMS@N,S-ACTs

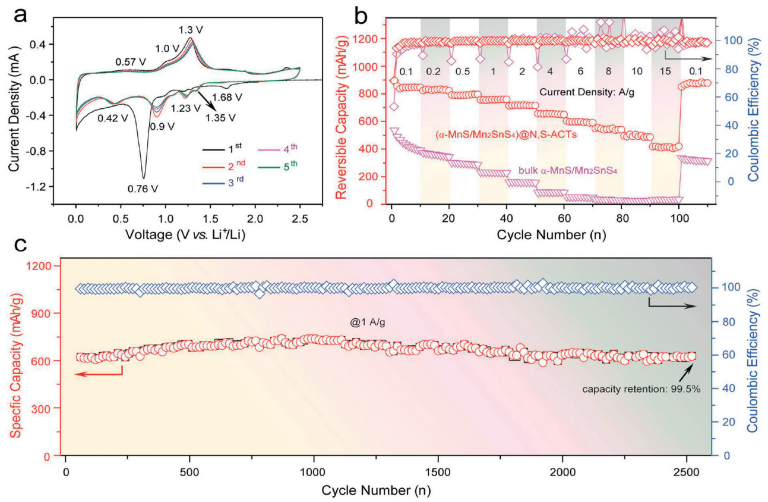

Fig. 4. Electrochemical characterizations for LIBs half cells. (a) CV curves at a scan rate of 0.1 mV/s of *h*-MMS@N,S-ACTs electrode. (b) The comparison of rate performance of *h*-MMS@N,S-ACTs and bulk *h*-MMS NWs electrodes. (c) The cycle performance after firstly three cycles at 0.1 A/g of *h*-MMS@N,S-ACTs electrodes.

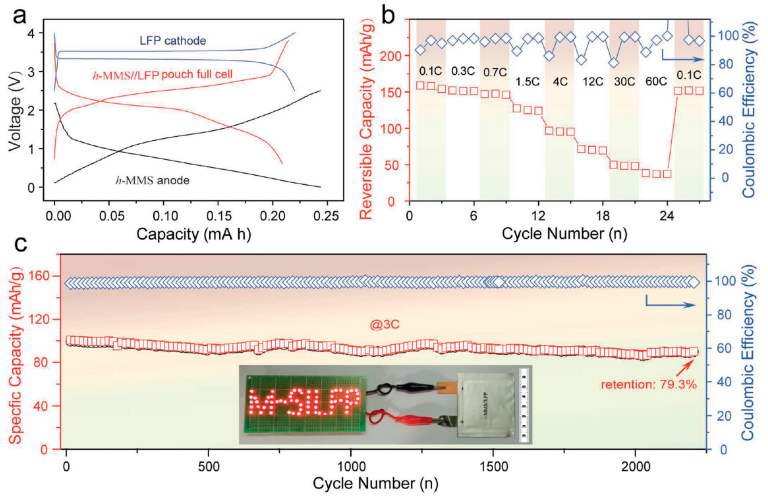

Fig. 5. Electrochemical characterizations for Li-ion pouch full cells. (a) The comparison of galvanostatic discharge/charge profiles of LFP cathode, *h*-MMS@N,S-ACTs anode and pouch *h*-MMS//LFP full cells. (b) The rate performance and (c) cycling performance at 3C of pouch *h*-MMS//LFP full cells. Inset of (c) shows that one fabricated Li-ion pouch full cell can lighten on a series LED. Note that: 1 C = 170 mAh/g.

electrode are predominated by pseudocapacitance, which should be responsible for the excellent conductivity network, nanostructured heterostructure of *h*-MMS@N,S-ACTs and benefit from the synergy of *h*-MMS, N,S- ACTs and high activated SSA. The pseudocapacitive behaviors of *h*-MMS@N,S-ACTs for Li-storage contribute to accelerate charge transfer, hence enhance the long-term cycling stability of electrodes (Fig. S16c in Supporting information). As shown in Fig. 4c, the *h*-MMS@N,S-ACTs electrode presents superior long-cycle life. A 618.3 mAh/g with the capacity retention of 99.5% can be obtained after 2500 cycles at 1 A/g, and the CE keeps ~100% except for the first three cycles (Fig. S17 in Supporting information). The specific capacity of *h*-MMS@N,S-ACTs is obvious superior to that of most reported Mn/Sn-based anodes for LIBs (Table S3). Moreover, as shown in Fig. S18 (Supporting information), the diameter of the nanotubes increased from 93–129 nm to 181–292 nm after 1000 cycles indicating that the volume expansion rate was about 95%–126%. The morphology of as-prepared *h*-MMS@N,S-ACTs is well retained after 1000 cycles (Fig. S18), which is benefiting from boosted nanoheterostructure architecture and the electrical connection between *h*-MMS core and N,S-ACTs shell.

In order to demonstrate the practicability of *h*-MMS@N,S-ACTs anode, the commercial $LiFePO_4$ (LFP) is used as the cathode material to couple with *h*-MMS@N,S-ACTs anode (henceforth denoted as *h*-MMS//LFP for pouch full-cell writing). The energy storage features of 6.5 cm × 5.8 cm *h*-MMS//LFP pouch full cells were evaluated by GDC analysis, rate and long cycle testing between 0.6–3.8 V. Fig. 5a shows the characteristic GDC curves of *h*-MMS anode, LFP cathode and *h*-MMS//LFP pouch full cells, respectively. Significantly, there is a slightly gradient charge and discharge plateaus at 2.95 and 2.05 V, respectively, which agree with the CV curves (Fig. S19 in Supporting information). Furthermore, the *h*-MMS//LFP pouch cell presents a high R_c of 158.8 mAh/g at 0.1 C (Fig. 5b). Even at a high rate of 12 C (300 s completed a discharge) and 30 C (120 s completed a discharge), a high R_c of 70.2 and 48.2 mAh/g can be obtained, respectively. In addition, the R_c could recover to 151.3 mAh/g when C-rates return to 0.1 C again, implying the reversible redox reaction. Most importantly, the *h*-MMS//LFP pouch full cell also shows ultra-long cycling stability (Fig. 5c). A high discharge C_s of 79.2 mAh/g with the capacity retention of 79.3% can be gained after 2200 cycles at 3 C. Meanwhile, the assembled 6.5 cm × 5.5 cm *h*-MMS//LFP pouch cell can light 64 series LED bulbs. The reversible long cycle life implies that the *h*-MMS@N,S-ACTs anode is a potential anode material for next-generation LIBs.

In summary, an effective design strategy, involving a nanostructured micro-pore heterostructure *h*-MMS encapsulation into N,S-ACTs, has been put forward. The structural features of *h*-MMS@N,S-ACTs heterostructures have been clarified via SEM, HRTEM, Raman, XPS characterizations and DFT calculation. When evaluated as anode electrode for Na-/Li-ion cells, the prepared *h*-MMS@N,S-ACTs exhibits excellent rate capability and cycling ability in Na-/Li-ion half cells and pouch full cells. These boosted energy storage performances are benefiting from the novel micro-pore *h*-MMS nanoheterostructure and enhanced ion/electron diffusion kinetics and conductivity, the superior rate and long cycling life of *h*-MMS@N,S-ACTs anode in Na-/Li-ion pouch full cells show that it is a hopeful anode candidate for next generation high-performance electrode materials.

Declaration of Competing Interest

The authors declare that they have no known competing financial interests or personal relationships that could have appeared to influence the work reported in this paper.

Acknowledgments

The authors D. Liu, H. Lü and X. Wu appreciate the financial support from the project funded by National Natural Science Foundation of China (Nos. 52372188, 51902090), 2023 Introduction of studying abroad talent program, Science Technology Program of Jilin Province (No. 20220508141RC), and the 111 Project (No. B13013), China Postdoctoral Science Foundation (No. 2019M652546), Henan Province Postdoctoral Start-Up Foundation (No. 1901017), Henan Normal University Doctoral Start-Up Project Foundation, "111" project (No. D17007) and Henan Center for Outstanding Overseas Scientists (No. GZS2018003). The author Z. Chen gratefully acknowledges the Dalian Revitalization Talents Program (No. 2022RG01), Natural Sciences and Engineering Research Council of Canada, the University of Waterloo, and the Waterloo Institute for Nanotechnology, University of Waterloo.

Supplementary materials

Supplementary material associated with this article can be found, in the online version, at doi:10.1016/j.cclet.2023.109285.

References

[1] B.K. Sovacool, Science 377 (2022) 478.
[2] W. Zhang, D.H. Seo, T. Chen, et al., Science 367 (2020) 1030–1034.
[3] M.J. Lee, J. Han, K. Lee, et al., Nature 601 (2022) 217–222.
[4] S. Ohno, W.G. Zeier, Nat. Energy 7 (2022) 686–687.
[5] Y. Jin, P.M.L. Le, P. Gao, et al., Nat. Energy 7 (2022) 718–725.
[6] J.M. Tarascon, Nat. Mater. 21 (2022) 979–982.
[7] J. Cao, L. Wang, D. Li, et al., Adv. Mater. 33 (2021) 2101535.
[8] P. Xiong, F. Zhang, X. Zhang, et al., Nat. Commun. 11 (2020) 3297.
[9] Y. Li, J. Zhang, Q. Chen, X. Xia, M. Chen, Adv. Mater. 33 (2021) 2100855.
[10] D. Yuan, Y. Dou, Y. Tian, et al., Angew. Chem. Int. Ed. 60 (2021) 18830–18837.
[11] X. Xiao, X. Duan, Z. Song, et al., Adv. Funct. Mater. 32 (2022) 2110476.
[12] X. Xie, X. Ma, Z. Yin, et al., Chem. Eng. J. 446 (2022) 137366.
[13] C. Hu, L. Chen, Y. Hu, et al., Adv. Mater. 33 (2021) 2103558.
[14] Y. Zheng, T. Zhou, C. Zhang, et al., Angew. Chem. Int. Ed. 55 (2016) 3408–3413.
[15] H.S. Zhao, K. Liang, S.J. Wang, et al., Adv. Sci. (2023) 2303696.
[16] E. Sanville, S.D. Kenny, R. Smith, G. Henkelman, J. Comput. Chem. 28 (2007) 899–908.
[17] A. Kostov, B. Friedrich, D. Zivkovic, Comput. Mater. Sci. 37 (2006) 355–360.
[18] X. Zhou, L. Yu, X.Y. Yu, X.W.D. Lou, Adv. Energy Mater. 6 (2016) 1601177.
[19] J.G. Wang, B. Wei, F. Kang, RSC Adv. 4 (2014) 199–202.
[20] D. Chen, H. Quan, G.S. Wang, L. Guo, Chempluschem 78 (2013) 843–851.
[21] M. Partik, T. Sting, H.D. Lutz, Z. Anorg, Allg. Chem. 621 (1995) 1600–1604.
[22] H. Wang, X.H. Zhang, X.H. Li, et al., Renewables 1 (2023) 353–361.
[23] K. Liang, H. Zhao, J. Li, et al., Small 19 (2023) 2207562.
[24] H.B. Wang, L. Li, W.Z. Han, et al., Renewables 1 (2023) 253–265.
[25] K. Liang, H. Zhao, J. Li, et al., Appl. Surf. Sci. 615 (2023) 156412.
[26] D.H. Liu, W. Li, F. Wan, et al., ChemElectroChem 3 (2016) 1354–1359.
[27] Y. Sun, X. Hu, W. Luo, F. Xia, Y. Huang, Adv. Funct. Mater. 23 (2013) 2436–2444.
[28] H.S. Zhao, Y.L. Qi, K. Liang, et al., Rare Metals 41 (2021) 1284–1293.
[29] K. Kravchyk, L. Protesescu, M.I. Bodnarchuk, et al., J. Am. Chem. Soc. 135 (2013) 4199–4202.
[30] D.H. Liu, W.H. Li, Y.P. Zheng, et al., Adv. Mater. 30 (2018) 1706317.